# Direct Numerical Simulation of a Wind-Generated Water Wave


**Jonas Steigerwald, Jonathan Reutzsch, Matthias Ibach, Martina Baggio, Adrian Seck, Brian K. Haus, and Bernhard Weigand**

**Abstract** The interaction between an airflow and a water surface influences many environmental processes. For example in a rough ocean, entrained droplets from the water surface enhance transport processes above the ocean surface which can lead to the formation of hurricanes. In order to get a better understanding of the fundamental processes we perform direct numerical simulations (DNS) of a wind-generated water wave. To conduct these simulations we use our in-house code Free Surface 3D (FS3D) which is based on the Volume-of-Fluid (VOF) method and uses a Piecewise Linear Interface Calculation (PLIC) method. Two simulations with different grid resolutions are presented. In both cases a gravity-capillary wind-wave develops, starting with a quiescent water surface and solely driven by the turbulent air flow. We evaluate different aspects of the wind-wave characteristics such as topology, phase velocity, and temporal development of the wave energy. Furthermore, we compare the results with linear wave theory and experimental data obtained in the ASIST wave tank of the University of Miami. The comparison shows a very good agreement between experiments and numerical predictions, thus, FS3D is capable of numerically reproducing a gravity-capillary wind-wave with high accuracy. In addition, we continued our work to optimize the performance of FS3D by replacing large pointer arrays in our code with allocatable arrays. The analysis of strong and weak scaling shows an improvement in performance of up to 48%.

J. Steigerwald (✉) · J. Reutzsch · M. Ibach · M. Baggio · A. Seck · B. Weigand
Institute of Aerospace Thermodynamics (ITLR), University of Stuttgart, Pfaffenwaldring 31, 70569 Stuttgart, Germany
e-mail: jonas.steigerwald@itlr.uni-stuttgart.de

B. K. Haus
Department of Ocean Sciences, Rosenstiel School of Marine and Atmospheric Science, University of Miami, 4600 Rickenbacker Causeway, Miama, FL, USA
e-mail: haus@rsmas.miami.edu



W. E. Nagel et al. (eds.), *High Performance Computing in Science and Engineering '19*,
https://doi.org/10.1007/978-3-030-66792-4_22

## 1 Introduction

The interaction between an airflow and a water surface is highly relevant for many environmental processes. When the airflow speed is high enough, droplets are entrained from the water surface, a scenario which is for example important for the formation and amplification of hurricanes. The intensity of such tropical cyclones depends on mass, momentum, and energy transfer between the air and the water and, thus, on size and number of entrained droplets. In order to get a reliable prediction of the intensity, an accurate estimation of the droplet size distribution in the sea spray environment is of great importance. However, the actual process of droplet entrainment is still not fully understood [31]. Precise experimental measurements of this small-scale process under such extreme conditions are hard to accomplish. Thus, our longterm objective is to uncover the mechanism of droplet entrainment from short wind-generated water waves by means of direct numerical simulation (DNS). In order to achieve this objective we use our in-house multiphase computational fluid dynamics (CFD) code Free Surface 3D (FS3D). FS3D is based on the Volume-of-Fluid (VOF) method and has already been used successfully to simulate complex hydrodynamic multiphase problems with droplet generation processes like primary jet breakup, droplet-wallfilm interactions, and droplet-droplet collisions [5, 6, 14, 19]. The first step towards our objective is the topic of this work: The generation of a pure wind-generated water wave, also called wind-wave, by using FS3D.

A DNS of a wind-wave is an ambitious task. Due to the high demands for the spatial and temporal resolution limits, the wind-speed, and the wavelength of wind-waves, the use of supercomputers is indispensable even today. One of the first DNS of a wind-wave in which both water and air layer were simulated was performed by Fulgosi et al. [8]. In their work they investigated the turbulent structures in the air above a deformable water surface. Both layers were driven by pressure gradients in opposite directions resulting in a countercurrent air-water flow. The surface elevation in their simulation was, however, only minimal due to the coarse mesh resolution. The same approach was used by Lakehal et al. [17] to evaluate the turbulent heat transfer across the deformable interface. Komori et al. [15] investigated a sheared gas-liquid interface due to wind-driven turbulence and the resulting turbulent structures in both water and air layer. In their simulations they initialized a fully developed wall turbulent airflow above a quiescent water layer. Furthermore, they used an arbitrary Lagrangian-Eulerian formulation (ALE) method with a moving grid.

The wind-wave generation process was investigated by Lin et al. [18]. Their air and water layer were separated by a deformable interface and they initialized a small constant velocity in the air layer to drive the waves. In addition, they superimposed the temperature field of both layers with small random perturbations to trigger turbulence caused by a distorted buoyancy force in normal direction to the interface. The very beginning of the wind-wave generation was investigated by Zonta et al. [32] with a countercurrent air-water flow.

The scalar transfer across an interface in a sheared wind-driven liquid flow and the effects of turbulent eddies, Langmuir circulation, and the influence of the Schmidt

number was studied by Takagaki et al. in [27, 28], respectively. In both studies, the numerical procedure was the same as used by Komori et al. [15]. A very topical simulation was performed by Hafsi et al. [10] who focused on the scalar transfer across the interface during onset and growth of small-scale Langmuir circulations. They followed closely the numerical approach of Komori et al. [15] as well.

In this paper, a similar approach to Lin et al. [18] is used to generate a wind-wave. However, no perturbations are superimposed on any field to guarantee that the onset of wave generation starts naturally and only due to the transition from the initial laminar air flow to a turbulent one. In contrast to all above mentioned works, we also evaluate the temporal development of the wave energy to determine the actual wave state and its development. Consequently, we are able to link occurring phenomena to the wave state. In order to estimate the necessary resolution of our computational grid, we perform two simulations using a coarse grid and a fine grid with a doubled number of grid cells in each direction. The resolution of the coarse grid is already finer as the resolution used by Hafsi et al. [10]. Thus, to the best of our knowledge, our investigation is the highest resolved simulation of a wind-wave so far. Since a good parallel performance of FS3D is essential for performing DNS on thousands of cores, we also continued the work of Reutzsch et al. [24] to convert all data fields with a pointer attribute to allocatable arrays. The results are also presented in this paper.

## 2 Formulation and Numerical Method

In order to solve the incompressible Navier–Stokes equations for multiphase flows by means of DNS the CFD code FS3D is used. It was developed at the Institute of Aerospace Thermodynamics (ITLR) in Stuttgart for more than 20 years and is continuously enhanced. A wide variety of recent studies demonstrates the ability to simulate highly dynamic processes and complex topologies [5, 6, 14, 19, 24]. Since small-scale turbulent fluctuations are directly resolved without utilizing turbulence modeling, a high resolution in space and time needs to be achieved. Therefore, simulations in FS3D are parallelized using MPI and OpenMP and were executed at the High-Performance Computing Center Stuttgart (HLRS) satisfying the high demand for computational power. FS3D is well validated on the Cray XC40 Hazel Hen supercomputer and shows good performance even in test cases with up to eight billion computational cells.

### *2.1 Numerical Method*

The in-house code FS3D solves the conservation equations for mass and momentum

$$\rho_t + \nabla \cdot (\rho \mathbf{u}) = 0, \tag{1}$$

$$(\rho \mathbf{u})_t + \nabla \cdot (\rho \mathbf{u} \otimes \mathbf{u}) = \nabla \cdot (\mathbf{S} - \mathbf{I}p) + \rho \mathbf{g} + \mathbf{f}_\gamma \tag{2}$$

on finite volumes (FV), where $\rho$ denotes the density, $\mathbf{u}$ the velocity vector, $p$ the static pressure; $\mathbf{g}$ denotes volume forces, such as gravity, and $\mathbf{f}_\gamma$ accounts for the body force which is used to model surface tension in the vicinity of the interface. The shear stress tensor $\mathbf{S}$ is defined by $\mathbf{S} = \mu \left[\nabla \mathbf{u} + (\nabla \mathbf{u})^T\right]$ for Newtonian fluids with $\mu$ representing the dynamic viscosity. The flow field is computed by solving equations (1) and (2) in a one-field formulation where the different phases are regarded as a single fluid with variable physical properties that discontinuously change across the separating interface. To identify the different phases, an additional indicator variable $f$ according to the classical VOF-method by Hirt and Nichols [11] is introduced. The VOF-variable $f$ determines the liquid volume fraction in each control volume and is defined as

$$f(\mathbf{x}, t) = \begin{cases} 0 & \text{in the gaseous phase,} \\ ]0;\, 1[ & \text{at the interface,} \\ 1 & \text{in the liquid phase.} \end{cases}$$

The scalar $f$ is advected across the computational domain by using the transport equation

$$f_t + \nabla \cdot (f \mathbf{u}) = 0. \tag{3}$$

Consistent with the one-field formulation, the local variables, e.g. the density, is defined by using the volume fraction $f$ and the respective values of a pure gaseous (index $g$) and liquid (index $f$) phase in our present case, resulting in

$$\rho(\mathbf{x}, t) = \rho_f f(\mathbf{x}, t) + \rho_g \left(1 - f(\mathbf{x}, t)\right). \tag{4}$$

To prevent numerical diffusion of the transport variable $f$ and to calculate the corresponding fluxes, FS3D makes use of a Piecewise Linear Interface Calculation algorithm (PLIC) proposed by Rider and Kothe [25]. The algorithm reconstructs a plane separating the fluid and the gas phase in an interface cell and is therefore capable of creating a sharp liquid-gas interface. For the advection method, three one-dimensional non-conservative transport equations are solved successively. With a permutation of the equation sequence and a specific divergence correction, second-order accuracy in space and time can be achieved [26]. Several models to compute the surface tension force are available. In the present study we use the conservative continuous surface stress (CSS) model by Lafaurie et al. [16]. A more detailed overview of the numerical implementation and methods as well as further capabilities and applications of FS3D are given in Eisenschmidt et al. [5].

### 2.2 Classification and Characterization of Wind-Waves

A classification of water waves can be achieved by considering the two acting restoring forces which return a displaced water surface to its equilibrium position: gravity and surface tension. The ratio of these forces is often used in context of water waves and is described by the non-dimensional Bond number

$$Bo = \frac{\Delta\rho g}{\sigma k^2}, \tag{5}$$

where $\Delta\rho = \rho_f - \rho_g$ and $k = 2\pi/\lambda$ is the wave number [30]. For $Bo \gg 1$ surface tension forces can be neglected and the main acting force is gravity. These waves are commonly referred to as gravity waves. For $Bo \ll 1$ surface tension forces become dominant and they are called capillary waves. Waves that lie in the transitional region where both forces have to be considered are referred to as capillary-gravity waves. This type of wave is simulated in this work.

Based on the wavelength $\lambda$, waves are governed by different physical processes and have different velocities of propagation $c$ which is expressed by the linear dispersion relation

$$c^2 = \frac{g}{k} + \frac{\sigma}{\rho_f} k. \tag{6}$$

Another important parameter for characterizing the current state of a propagating wave is the total wave energy content per surface area $E_{wave}$ as given by Tulin [29] consisting of the sum of three energy components, resulting in

$$E_{wave} = E_{kin} + E_{pot} + E_{\sigma}. \tag{7}$$

The energy components in Eq. (7) are the kinetic energy $E_{kin}$ of the water, the gravitational potential energy $E_{pot}$ with respect to the initially flat water surface, and the surface energy $E_{\sigma}$. A detailed description of the energy components can be found in Kaufmann [13].

## 3 Numerical Setup

The wind-waves are simulated using a three-dimensional rectangular computational domain with dimensions $\lambda \cdot 0.5\lambda \cdot 2\lambda$ in streamwise, spanwise, and normal direction, respectively, as shown in Fig. 1. The wavelength $\lambda$ is set to $\lambda = 0.05$ m which ensures that the generated wind-waves lie within the range of gravity-capillary waves. The domain consists of an initially quiescent water layer and an air layer with an initial velocity of $U = 15$ m/s in streamwise direction. Both water and air layer have thickness $\lambda$. For the water layer this guarantees that a generated wave is not influenced by the bottom, meaning that the deep water assumption $d > 0.5\lambda$ is fulfilled [1]. The

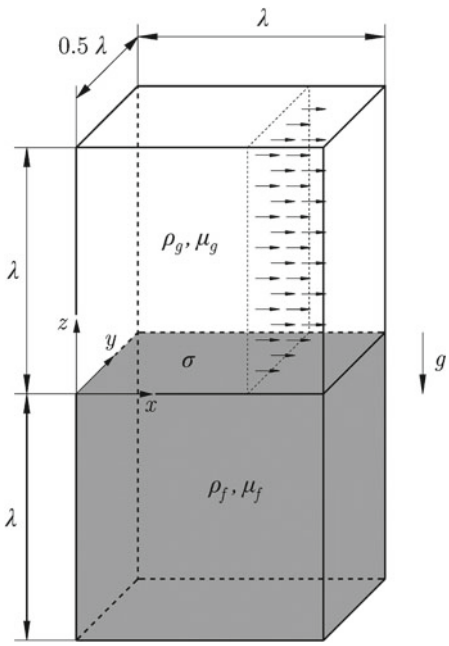


**Fig. 1** Computational domain and coordinate system. The arrays in the air layer indicate the initial direction of the wind

chosen thickness of the air layer ensures on the one hand that the air flow contains sufficient kinetic energy to accelerate the water surface and to become turbulent, leading to the generation of a wind-wave. It should be mentioned, that since the total energy of the system consists only of kinetic energy at the beginning, the air velocity is freely-decaying during the simulation due to the energy transfer into the water layer. On the other hand we can ensure that the interaction between the turbulent air flow and the water surface is not disturbed by the upper boundary of the computational domain. At the upper boundary as well as at the bottom of the domain free slip boundary conditions are applied, whereas in streamwise and spanwise direction periodic boundary conditions are used.

In this study, two different grid resolutions are used in order to analyze the necessary grid resolution for simulating accurately a gravity-capillary wind-wave. For the simulation with the coarse resolution we discretize the domain with an equidistant Cartesian grid using $256 \cdot 128 \cdot 512$ cells. For the fine resolution the number of cells is doubled in each direction leading to $512 \cdot 256 \cdot 1024$ cells. Therefore, the number of used processors is 512 for the coarse and 2048 for the fine grid resolution, respectively.

For both simulations the physical properties of air and fresh water are used at reference temperature $T = 293\,\mathrm{K}$ and standard pressure $p = 1.013$ bar. The properties are listed in Table 1. By using these physical properties and the selected wavelength the Bond number results in $Bo = 8.52$ indicating that surface tension already plays a significant role in our simulations and must not be ignored.

**Table 1** Physical properties of air and water

| Air density $\rho_g$ (kg/m$^3$) | Air viscosity $\mu_g$ (Ns/m$^2$) | Water density $\rho_f$ (kg/m$^3$) | Water viscosity $\mu_f$ (Ns/m$^2$) | Surface tension $\sigma$ (N/m) |
|---|---|---|---|---|
| 1.204 | $1.813 \times 10^{-5}$ | 998 | $1.002 \times 10^{-3}$ | $72.74 \times 10^{-3}$ |

In order to show that the grid resolution is sufficient for DNS, we calculated the ratio of grid spacing $\Delta x$ to the smallest dissipative length scale, the Kolmogorov length ($\Delta x_{coarse}/l_{k,coarse} = 9.89$, $\Delta x_{fine}/l_{k,fine} = 5.11$). The chosen characteristic velocity is the highest velocity at the point in time when a single wave has formed. Since both grid spacing and Kolmogorov length are in the same order of magnitude for both grids, we are able to produce physically correct results.

## 4 Results

In the following the results of both simulations are compared regarding the overall shape, the phase velocity, and the wave energy. In addition, we compare the simulation on the fine grid with experimental data. For the evaluation, the non-dimensional time

$$\tilde{t} = \frac{tc}{\lambda} \tag{8}$$

was introduced, where $c$ is the phase velocity, Eq. (6), for the corresponding wavelength. Both simulations were performed until $\tilde{t} = 7$ was reached meaning that the wave could run seven times through the computational domain. It is important to mention is that the growth of the waves at the early stages is influenced by the periodicity of the computational domain. For this reason, the results are not taken into account until a single wave has formed at $\tilde{t} \approx 4$.

In Fig. 2 both simulated gravity-capillary wind-waves are shown at three different times $\tilde{t} = 5$, $\tilde{t} = 6$, and $\tilde{t} = 7$. On the left side, Fig. 2a–c show the result using the coarse grid, whereas on the right side, Fig. 2d–e depict the wind-wave using the fine grid. For both cases the VOF-variable $f$ is depicted as a contour plot, showing the iso-surface through $f = 0.5$ representing the water surface. Furthermore, the velocity magnitude is depicted on two slices in streamwise and spanwise direction, respectively. As one can see, for both resolutions a wind-wave has emerged showing the typical shape of a gravity-capillary wave with a pronounced bulge on the top of the wave's leeward side, caused by surface tension effects [4, 20]. Both waves are driven by a turbulent air flow above the water. In both cases a decrease of the velocity magnitude over time is visible due to dissipation effects and energy transfer from air to water. The turbulence structures as well as the recirculation region above the waves' leeward side is, however, more pronounced for the fine simulation, as expected. In addition, a clear difference on the leeward side between both simulations

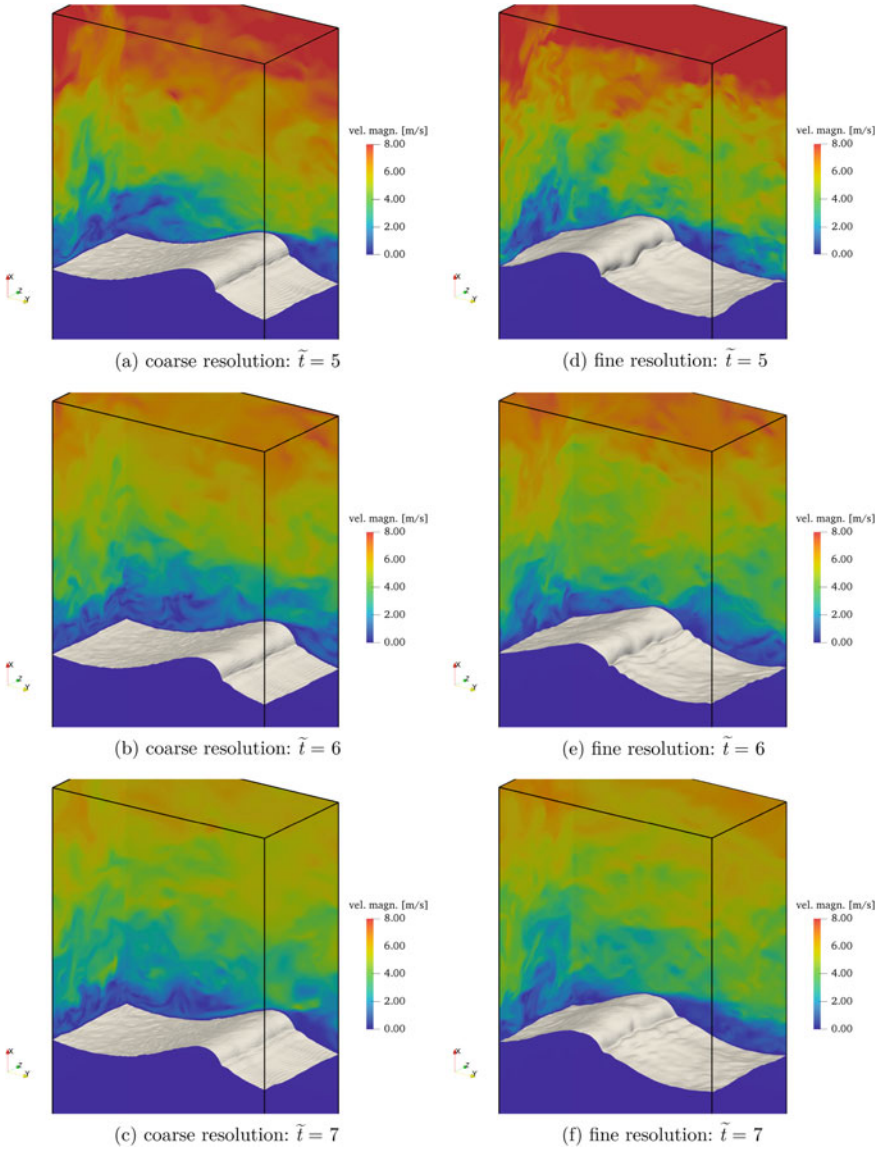


**Fig. 2** Comparison of the simulated gravity-capillary wind-wave using the coarse mesh resolution **a**–**c** (left) and the fine mesh resolution **d**–**f** (right) for $\tilde{t} = 5$, $\tilde{t} = 6$, and $\tilde{t} = 7$

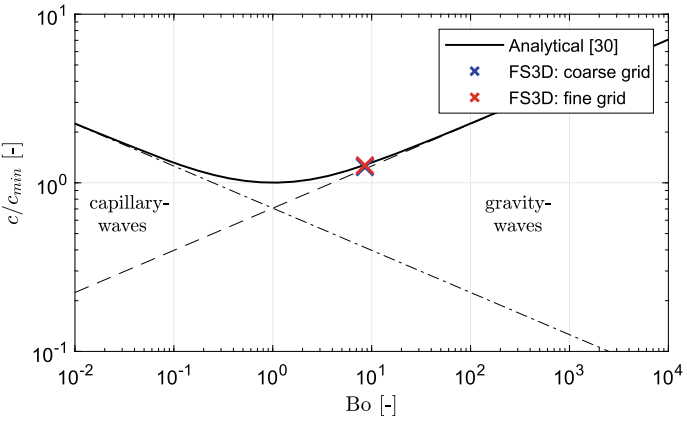


**Fig. 3** Comparison of the evaluated phase velocity of both simulated wind-waves with analytical values from the linear wave theory, see Eq. (6) [30]. The phase velocity was evaluated between $\tilde{t} = 6$ and $\tilde{t} = 7$ and was made non-dimensional by means of $c_{min} = (4g\sigma/\rho_f)^{1/4}$

is visible. The fine resolved wind-wave shows a well-developed train of smaller waves on the forward face of the wave. In context of physical oceanography these small waves are called "parasitic[1] capillary waves". We will make use of this expression in the following. The parasitic capillary waves remain stationary in the frame of the moving wind-wave and are characteristic of gravity-capillary waves [20]. Down the forward side of the wave they finally disappear due to viscous damping [2]. The coarse resolved wave shows in contrast only one weak developed parasitic capillary wave indicating that the grid resolution is insufficient to accurately reproduce all characteristics of the gravity-capillary wind-wave.

To verify that the propagation of the wind-waves can be numerically reproduced we evaluated their phase velocity between $\tilde{t} = 6$ and $\tilde{t} = 7$ and compared the values with the analytical solution from the linear wave theory (Eq. (6)). This time interval was selected since the energy input by the wind is low during this interval and, therefore, the wave comes closest to a state of equilibrium. The point of reference for the evaluation was at both times the location of the maximum surface elevation averaged over the width of each wave. The resulting velocities are shown in Fig. 3 in non-dimensional form by scaling with the smallest possible phase velocity after the linear wave theory of $c_{min} = (4g\sigma/\rho_f)^{1/4}$ [30]. As can be seen, the phase velocity of the simulated wind-waves for both coarse and fine grid are nearly identical to the analytical solution. The deviation between the fine grid solution and the analytical solution is only around 0.8%, whereas the coarse grid solution overestimates the analytical solution by 2.6%. Even though these small deviations are present, this

[1]The term "parasitic" in context of physical oceanography must not be confused with the term "parasitic" in CFD simulation, where it describes artificial perturbations due to discretization errors leading to unphysical effects.

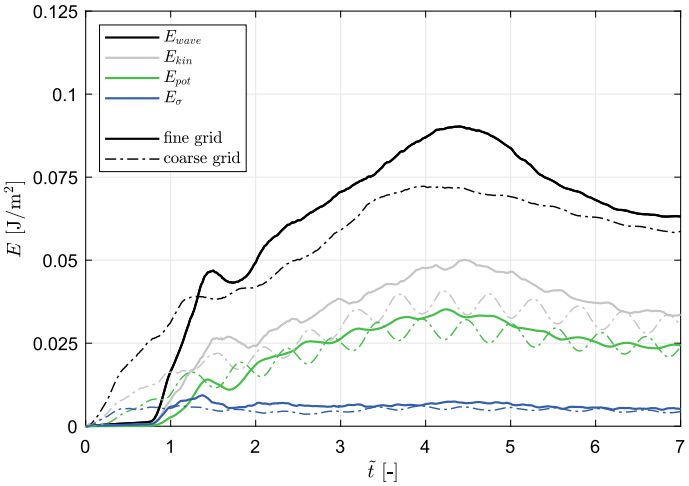


**Fig. 4** Temporal evolution of the total wave energy and its three components for the coarse (dash-dotted lines) and fine (solid lines) computational grid

result clearly shows that our simulated wave exhibits a reasonable phase velocity and that already the coarse grid is sufficient to reproduce the velocity of wave propagation.

Besides the decreasing air flow velocity, also the bulge and the parasitic capillary waves seem to recede over time. This behavior can be explained by looking at the temporal evolution of the total wave energy which is shown together with its three energy components for both simulated wind-waves in Fig. 4. For both waves the temporal development of the wave energy is similar and differs only in few aspects. All energy components increase moderately and reach a maximum at $\tilde{t} = 4$ and $\tilde{t} \approx 4.4$ depending on the grid resolution. The maxima coincidence with the moment a single wind-wave has formed. After that, the energy decreases, however, differently strong for both grid resolutions. This energy decrease can be clearly linked now to the occurrence and recession of the parasitic capillary waves. Parasitic capillary waves extract energy from the main wave, enhance damping effects due to viscous dissipation, and, therefore, influence the dispersive and dissipative properties of the underlying main wave [7]. In case of the coarse grid resolution, the total wave energy $E_{wave}$ decreases almost linear, as can be seen in Fig. 4. This is a consequence of the low resolved parasitic capillary wave whose shape remains nearly the same over time and whose dissipative effects cannot be numerically reproduced accurately. In contrast, for the simulation on the finer grid the decrease of the total wave energy $E_{wave}$ shows strong nonlinear behavior caused by the dynamical behavior of parasitic capillary waves which was made possible due to fine grid resolution.

In order to show the physical soundness of our simulated gravity-capillary wind-wave, we compared our fine resolved simulation with our experimental data obtained by Ibach [12]. The experiments on short wind-waves were conducted in the Air-

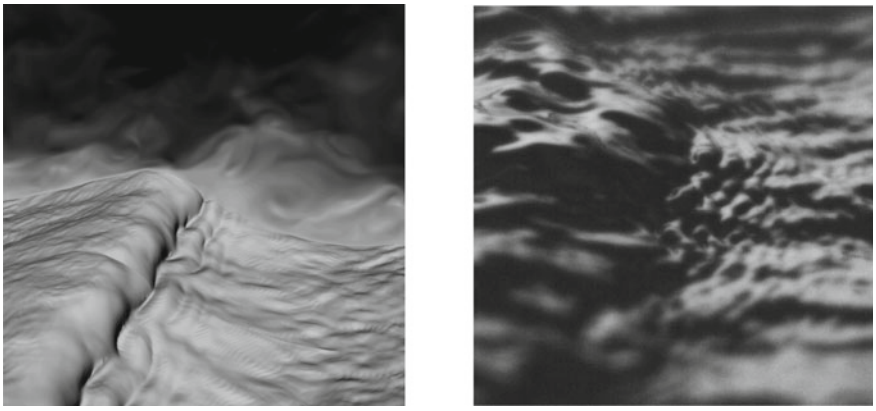

**Fig. 5** Comparison of the simulated gravity-capillary wind-wave using the fine mesh (left) with experimental work by Ibach [12] (right). The train of parasitic capillary waves on the leeward side of the wind-wave can be numerically reproduced using FS3D

Sea Interaction Salt Water Tank (ASIST) of the University of Miami. A detailed description of the experimental setup can be found in [3, 12, 21, 22].

Figure 5 shows two close-up views of the leeward side of a wind-wave for both simulation on the lefthand side at $\tilde{t} = 6$ and experiment on the right hand side. As one can see, there is a good agreement between the simulated wind-wave with the fine structures on the wave's forward face and the observed wind-wave from the experiments. Both show a pronounced train of parasitic capillary waves in front of the bulge. From this result clearly follows, that only by using the fine grid resolution it is possible to simulate a gravity-capillary wind-wave and to reproduce important aspects of such a wave, as can be observed in wind-wave environments. It is also important to mention that the wavelengths of the parasitic capillary waves in simulation and experiment in Fig. 5 are not of the same size. The section visible in the experiment (see Fig. 5) is around 4 cm in the focal plane and shows only a part of the wind-wave. The wavelength of the observed complete wind-wave in the wave tank is, therefore, slightly longer than the one of our simulated wave. In contrast, the wavelength of the parasitic capillary waves in the experiment are shorter than the ones in our simulation. This observed relationship is as expected, since the wavelength of the parasitic capillary waves depends on the wavelength of the complete wind-wave due to the resonant condition and the linear dispersion relation [7]: The longer wavelength of the complete water wave, the shorter the wavelength of its parasitic capillary waves. This fact as well as the presence of the parasitic capillary waves indicate the good quality of our fine resolved gravity-capillary wind-wave. However, further simulations have to be performed in the future using finer grid resolutions in order to clarify if the train of capillary waves seen in the here presented simulation is sufficiently resolved.

# 5 Computational Performance

## 5.1 Dynamic Memory Allocation: Pointer Versus Allocatable Arrays

As reported by Reutzsch et al. [24], most of FS3D dynamic arrays have been declared with a pointer attribute for historical reasons. In contrast to allocatable arrays, objects with the pointer attribute can refer to different memory addresses during runtime. Because of this feature, pointer objects have more capabilities with respect to their allocatable counterpart, but they can also hinder optimization from the compiler so that a massive use of pointer arrays can result in a slower code. This was the reason that led us to switch from pointer to allocatable arrays wherever possible. This operation, already initiated in 2018 [24], has been finalized this year.

In the following, we present a performance analysis for this optimized version in terms of cycles per hour and code scalability. The benchmark case, analogous to the one described in [24], is an oscillating droplet representing a spume droplet entrained from a short wind-wave at high wind speeds. The droplet is initialized as an ellipsoid with the semi-principal axis $a = b = 1.357\,\text{mm}$ and $c = 0.543\,\text{mm}$ at the center of a cubic domain with an edge length of $x = y = z = 8\,\text{mm}$. The fluid of the droplet is water at $T = 293\,\text{K}$. We measured the performance of both weak and strong scaling, where we varied the number of processors from $2^3$ up to $16^3$. Since we did not use hyperthreading, the number of processors corresponds to the number of processes. The details of the analysis setups are shown in Table 2 for the strong scaling and in Table 4 for the weak scaling. Here, we used only spatial domain composition with MPI parallelization. For information on FS3D performance with hybrid OpenMP and MPI operation see [9, 23].

## 5.2 Strong Scaling

All simulated cases shown in Table 2 were carried out with a duration of 25 min and with a constant processor clock rate of 2.5 GHz. From the number of cycles performed in each case, we estimated the number of cycles per hour (CPH), which in turn was used to calculate the strong scaling efficiency (SSE). The latter is defined as:

$$SSE = \frac{CPH_N}{N \times CPH_1}. \tag{9}$$

As we don‘t have a case with just one processor, equation (9) changes to

$$SSE = \frac{CPH_N}{N/8 \times CPH_8}. \tag{10}$$

**Table 2** Strong scaling setup

| Problem size | $512^3$ | | | |
|---|---|---|---|---|
| MPI-processes | $2^3$ | $4^3$ | $8^3$ | $16^3$ |
| Cells per process | $256^3$ | $128^3$ | $64^3$ | $32^3$ |
| Nodes | 2 | 4 | 32 | 256 |
| Processes per node | 4 | 16 | 16 | 16 |

**Table 3** Number of cycles per hour for the simulated cases

| Processors | CPH allocatable | CPH pointer |
|---|---|---|
| 8 | 79.2 | 64.2 |
| 64 | 403.2 | 364.8 |
| 512 | 2203.2 | 1994.4 |
| 4096 | 441.6 | 415.2 |

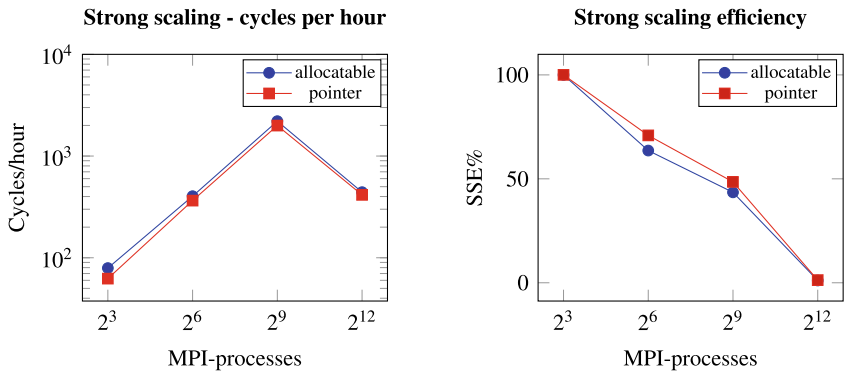


**Fig. 6** Number of cycles per hour (on the left) and strong scaling efficiency (on the right) over the number of processes for the code versions with allocatable and pointer arrays

The results for the strong scaling test are shown in Table 3 and in Fig. 6. It can be seen that both code versions exhibit similar trends both in terms of cycles per hours and code scalability, whereas the code version with allocatable arrays is slightly faster for all simulated cases. The peak performance in terms of CPH is obtained in the 512 processors case, where the code version with allocatable arrays is about 10% faster (Table 3).

**Table 4** Weak scaling setup

| Cells per process | $64^3$ | | | |
|---|---|---|---|---|
| Problem size | $128^3$ | $256^3$ | $512^3$ | $1024^3$ |
| MPI-processes | $2^3$ | $4^3$ | $8^3$ | $16^3$ |
| Nodes | 2 | 4 | 32 | 256 |
| Processes per node | 4 | 16 | 16 | 16 |

**Table 5** Number of cycles per hour for the simulated cases

| Processors | CPH allocatable | CPH pointer |
|---|---|---|
| 8 | 4428.794 | 3700.332 |
| 64 | 2893.369 | 2674.084 |
| 512 | 2142.857 | 1990.533 |
| 4096 | 300.592 | 203.283 |

## *5.3 Weak Scaling*

The weak scaling was performed in analogy to the strong scaling. The simulations were carried out for 25 min with a constant processor clock rate (2.5 GHz). From that, the estimated number of cycles per hour (CPH) is used to calculate the weak scaling efficiency (WSE), defined by (11)

$$WSE = \frac{CPH_N}{CPH_1}. \tag{11}$$

Again, we don‘t have a case with just one processor, therefore equation (11) changes to

$$WSE = \frac{CPH_N}{CPH_8}. \tag{12}$$

Table 5 gives the number of cycles per hour for each simulation. Overall, the code version with the allocatable arrays is faster than the old version with pointers (see Fig. 7, left). For the small case with 8 processors ($128^3$ cells) a speed-up of 19.7% could be achieved. The difference is decreasing for larger cases up to a number of processes of 512 ($512^3$ cells), where the version with the pointers is 7.7% slower. Calculations with more processors, in this case 4096 ($1024^3$ cells), the total number of cycles per hour is decreasing drastically for both versions. This can also be seen when looking at the weak scaling efficiency in Fig. 7 on the right. However, the version with allocatable arrays is loosing less performance and, therefore, ends up with 47.9% more cycles per hour than the version with pointers.

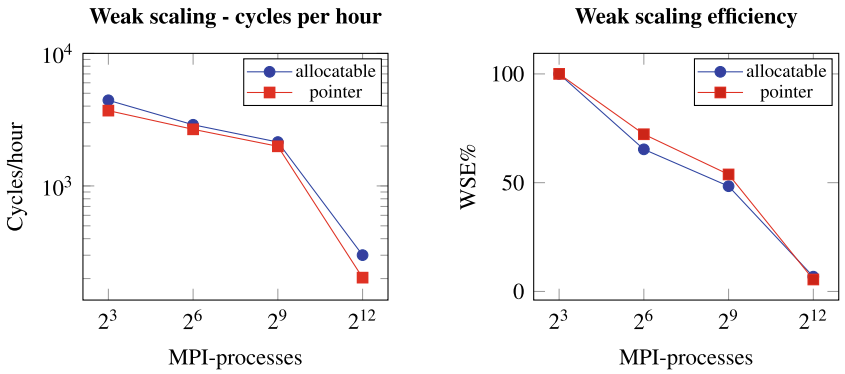


**Fig. 7** Number of cycles per hour (on the left) and weak scaling efficiency (on the right) over the number of processes for the code versions with allocatable and pointer arrays

## 6 Conclusions

We presented our first DNS of a pure wind-generated water wave performed with the in-house code FS3D, which is based on the VOF- and PLIC-method. Whereas in most other studies dealing with this topic the initial wave structure or initial turbulence is imposed artificially, we set up a framework with a complete quiescent water layer and an air layer with a velocity profile. With this approach we ensure a natural generation of the wind-wave from scratch, only restricted to the applied domain length, hence, we chose only the final wavelength in advance. We performed two simulations of a wind-wave using a coarse and a fine grid resolution of the computational domain. We showed that in both cases a wind-wave has developed, solely driven by the turbulent air flow and with a typical shape of a gravity-capillary wave.

In both simulations the expected turbulent structures, the recirculation region on the leeward wave side and parasitic capillary waves could be identified. However, only with a fine grid resolution the dynamic behavior of the parasitic capillary waves could be captured. This was concluded by analyzing the temporal development of the wave energy. Furthermore, we verified the physical soundness of our simulation by making a comparison of the velocity of wave propagation to an analytical approach based on the linear wave theory. The evaluated phase velocity showed a good agreement for both simulations. As additional validation, we compared the simulation on the fine grid with experimental data obtained in the ASIST test rig of the University of Miami. A visual comparison of the topology and the wave type with a high speed camera image yielded promising results. For this reason, it is to planned increase the wind speed in future investigations in order to induce droplet entrainment from the water surface and to uncover the mechanism involved.

Furthermore, we finalized our work on replacing large pointer arrays in our Fortran code with allocatable arrays, which was initiated in our last report. Henceforth, with changing all possible pointers we conducted a full performance analysis, including

strong and weak scaling. Both evaluations proved a much better performance with the conversion from pointers to arrays in our code.

**Acknowledgements** The authors kindly acknowledge the *High Performance Computing Center Stuttgart* (HLRS) for support and supply of computational time on the Cray XC40 platform under the Grant No. FS3D/11142. In addition, the authors kindly acknowledge the financial support of the Deutsche Forschungsgemeinschaft (DFG) through the projects GRK 2160/1, SFB-TRR75, WE2549/36-1, and WE2549/35-1.

## References

1. R.G. Dean, R.A. Dalrymple, *Water Wave Mechanics for Engineers and Scientists*. Advanced Series in Ocean Engineering, Vol. 2 (World Scientific, 1991)
2. L. Deike, S. Popinet, W. Melville, Capillary effects on wave breaking. J. Fluid Mech. **769**, 541–569 (2015)
3. M.A. Donelan, B.K. Haus, W.J. Plant, O. Troianowski, Modulation of short wind waves by long waves. J. Geophys. Res.: Ocean. **115**(C10) (2010)
4. J.H. Duncan, Spilling breakers. Annu. Rev. Fluid Mech. **33**(1), 519–547 (2001)
5. K. Eisenschmidt, M. Ertl, H. Gomaa, C. Kieffer-Roth, C. Meister, P. Rauschenberger, M. Reitzle, K. Schlottke, B. Weigand, Direct numerical simulations for multiphase flows: an overview of the multiphase code FS3D. J. Appl. Math. Comput. **272**(2), 508–517 (2016)
6. M. Ertl, B. Weigand, Analysis methods for direct numerical simulations of primary breakup of shear-thinning liquid jets. At. Sprays **27**(4), 303–317 (2017)
7. A.V. Fedorov, W.K. Melville, Nonlinear gravity-capillary waves with forcing dissipation. J. Fluid Mech. **354**, 1–42 (1998)
8. M. Fulgosi, D. Lakehal, S. Banerjee, V. De Angelis, Direct numerical simulation of turbulence in a sheared air-water flow with a deformable interface. J. Fluid Mech. **482**, 319–345 (2003)
9. C. Galbiati, M. Ertl, S. Tonini, G.E. Cossali, B. Weigand, DNS investigation of the primary breakup in a conical swirled jet, in *High Performance Computing in Science and Engineering '15* (Transactions of the High Performance Computing Center, Stuttgart (HLRS), 2016), pp. 333–347
10. A. Hafsi, A.E. Tejada-Martínez, F. Veron, Dns of scalar transfer across an air-water interface during inception and growth of Langmuir circulation. Comput. Fluids **158**, 49–56 (2017)
11. C.W. Hirt, B.D. Nichols, Volume of fluid (VOF) method for the dynamics of free boundaries. J. Comput. Phys. **39**(1), 201–225 (1981). https://doi.org/10.1016/0021-9991(81)90145-5
12. M. Ibach, Investigations on sea spray generation and wave breaking processes on short wind waves. Master's thesis, University of Stuttgart, Institute of Aerospace Thermodynamics (2018)
13. J. Kaufmann, Direkte numerische Simulation der Instabilität einer überströmten Wasseroberfläche. Master's thesis, University of Stuttgart, Institute of Aerospace Thermodynamics (2016)
14. J. Kaufmann, A. Geppert, M. Ertl, R. Bernard, V. Vaikuntanathan, G. Lamanna, B. Weigand, Direct numerical simulations of one- and two-component droplet wall-film interactions within the crown-type splashing regime, in *ICLASS 2018, 14th triennial International Conference on Liquid Atomization and Spray Systems*, Chicago, USA (2018)
15. S. Komori, R. Kurose, K. Iwano, T. Ukai, N. Suzuki, Direct numerical simulation of wind-driven turbulence and scalar transfer at sheared gas-liquid interfaces. J. Turbul. **11**, N32 (2010)
16. B. Lafaurie, C. Nardone, R. Scardovelli, S. Zaleski, G. Zanetti, Modelling merging and fragmentation in multiphase flows with SURFER. J. Comput. Phys. **113**(1), 134–147 (1994)
17. D. Lakehal, M. Fulgosi, G. Yadigaroglu, S. Banerjee, Direct numerical simulation of turbulent heat transfer across a mobile, sheared gas-liquid interface. ASME J. Heat Transf. **125**(6), 1129–1139 (2003)

18. M.Y. Lin, C.H. Moeng, W.T. Tsai, P.P. Sullivan, S.E. Belcher, Direct numerical simulation of wind-wave generation processes. J. Fluid Mech. **616**, 1–30 (2008)
19. M. Liu, D. Bothe, Numerical study of head-on droplet collisions at high weber numbers. J. Fluid Mech. **789**, 785–805 (2016)
20. M.S. Longuet-Higgins, The generation of capillary waves by step gravity waves. J. Fluid Mech. **16**, 138–159 (1963)
21. L. Muser, Experimental and numerical investigations of sea spray generation processes on short wind waves. Master's thesis, University of Stuttgart, Institute of Aerospace Thermodynamics (2017)
22. D.G. Ortiz-Suslow, B.K. Haus, S. Mehta, N.J.M. Laxague, Sea spray generation in very high winds. J. Atmos. Sci. **73**(10), 3975–3995 (2016)
23. P. Rauschenberger, J. Schlottke, B. Weigand, A computation technique for rigid particle flows in an Eulerian framework using the multiphase DNS code FS3D, in *High Performance Computing in Science and Engineering '11*, Transactions of the High Performance Computing Center, Stuttgart (HLRS) (2011). https://doi.org/10.1007/978-3-642-23869-7_23
24. J. Reutzsch, M. Ertl, M. Baggio, A. Seck, B. Weigand, Towards a direct numerical simulation of primary jetbreakup with evaporation, in *High Performance Computing in Science and Engineering '18*, ed. by W.E. Nägel, D.H. Kröner, M.M. Resch (Springer International Publishing, 2019)
25. W.J. Rider, D.B. Kothe, Reconstructing volume tracking. J. Comput. Phys. **141**(2), 112–152 (1998). https://doi.org/10.1006/jcph.1998.5906
26. G. Strang, On the construction and comparison of difference schemes. SIAM J. Numer. Anal. **5**(3), 506–517 (1968)
27. N. Takagaki, R. Kurose, Y. Tsujimoto, S. Komori, K. Takahashi, Effects of turbulent eddies and Langmuir circulations on scalar transfer in a sheared wind-driven liquid flow. Phys. Fluids **27**(1), 016,603 (2015)
28. N. Takagaki, R. Kurose, A. Kimura, S. Komori, Effect of Schmidt number on mass transfer across a sheared gas-liquid interface in a wind-driven turbulence. Sci. Rep. **6**(37059) (2016)
29. M.P. Tulin, On the transport of energy in water waves. J. Eng. Math. **58**(1), 339–350 (2007)
30. J.M. Vanden-Broeck, *Gravity-Capillary Free-Surface Flows* (Cambridge University, 2010)
31. F. Veron, Ocean spray. Annu. Rev. Fluid Mech. **47**(1), 507–538 (2015)
32. F. Zonta, A. Soldati, M. Onorato, Growth and spectra of gravity-capillary waves in counter-current air/water turbulent flow. J. Fluid Mech. **777**, 245–259 (2015)